Applied Physics Letters

Antenna-coupled microbolometer based on VO_2's non-linear properties across the metal–insulator transition region

Cite as: Appl. Phys. Lett. **121**, 201901 (2022); https://doi.org/10.1063/5.0123779
Submitted: 01 September 2022 • Accepted: 28 October 2022 • Published Online: 15 November 2022

Shangyi Chen, Mark Lust and Nima Ghalichechian

AIP Publishing

Applied Physics Letters ARTICLE scitation.org/journal/apl

Antenna-coupled microbolometer based on VO_2's non-linear properties across the metal–insulator transition region

Cite as: Appl. Phys. Lett. **121**, 201901 (2022); doi: 10.1063/5.0123779
Submitted: 1 September 2022 · Accepted: 28 October 2022 ·
Published Online: 15 November 2022

Shangyi Chen,[1,2,a),b)] Mark Lust,[1] and Nima Ghalichechian[3]

AFFILIATIONS

[1]Department of Electrical and Computer Engineering, The Ohio State University, Columbus, Ohio 43212, USA
[2]Department of Mechanical and Aerospace Engineering, The Ohio State University, Columbus, Ohio 43212, USA
[3]School of Electrical and Computer Engineering, Georgia Institute of Technology, Atlanta, Georgia 30308, USA

[a)]**Author to whom correspondence should be addressed:** chen.6642@osu.edu
[b)]This research was performed while Shangyi Chen was at The Ohio State University, Columbus, Ohio 43212, USA.

ABSTRACT

This paper presents an antenna-coupled non-linear vanadium dioxide (VO_2) microbolometer operating in the non-linear metal–insulator transition (MIT) region with an ultra-high responsivity of 6.55×10^4 V/W. Sputtered VO_2 films used in this device exhibit 10^4 times change in resistivity between the dielectric and conductive states. The VO_2 microbolometer is coupled to a wideband dipole antenna operating at 31–55 GHz and a coplanar waveguide for probed measurement. To enhance the sensitivity, the sensor is suspended in air by micro-electro-mechanical systems process. The large thermal coefficient of resistance of VO_2 is utilized by DC biasing the device in the MIT region. Measurements for the fabricated sensor were performed, and a high responsivity was demonstrated, owing to non-linear conductivity change in the transition region. The measured sensitivity is $>10^2$ times higher than the state-of-the-art sensors. In addition, the concept of utilizing the proposed VO_2 sensor in a mmWave imager was demonstrated by the radiation pattern measurement of a 4×4 (16 elements) antenna-coupled VO_2 sensor array. The results presented in this work reveal the initial step to employ VO_2's MIT for a hyper-sensitive sensor in future mmWave sensing and imaging applications.

The exploration of the mmWave band defined by frequencies between 30 and 300 GHz (corresponding to the wavelengths of 10 and 1 mm, respectively) has been popularly pursued in recent years, with the advantages of high bandwidth and ability to see through common materials. Furthermore, there is an increasing demand for reconfigurable mmWave systems for their use in defense, satellite communication, 5G and beyond, switching, imaging, and sensing. Phase change materials (PCMs), which have tunable physical properties such as electrical resistivity and optical transmittance,[1] have attracted intensive focus to achieve low-loss mmWave microsystems.[2] In particular, vanadium dioxide (VO_2) belongs to PCMs and exhibits a metal–insulator transition (MIT) near room temperature (68 °C) with a stark resistivity change ($\sim 10^4$).[3]

The large or non-linear thermal coefficient of resistance (TCR) in the MIT region makes VO_2 a promising candidate for microbolometers, whose electrical resistance changes in response to the heat from radiation absorption, i.e., an antenna in our case. The bolometer was introduced in 1880.[4] It has been mostly implemented at infrared (IR)[5–8] because the emitted black body radiation has the highest amplitude in this region. The energy, however, reduces by 10^8 times at the mmWave band. Nevertheless, a mmWave imager can have $>10^5$ times better noise performance and $>10^3$ higher temperature contrast than IR detectors,[9–11] so it is possible to detect black body radiation at the mmWave band. Additionally, the ability to penetrate obstacles that obfuscate IR and visible radiation (e.g., fog or clothes) makes mmWave cameras useful in both day and night operation as well as in other low-visibility conditions that limit the capability of IR and visible light cameras.[12]

Considering that the output responsivity of the microbolometer is directly proportional to the TCR of the sensitive material, it is beneficial to employ a material like VO_2 with a high TCR. The conventionally used sensitive materials in the microbolometer are linear,[13] such as niobium,[6,14] titanium,[15] nickel,[16] bismuth,[17] and platinum,[18] whose TCR values are generally low and are 0.1–0.4%/K. Vanadium oxide

(VO_x) has only been utilized in the dielectric phase for imaging cameras with a TCR of −2 to −2.4%/K.[19,20] One major bottleneck of using VO_2 has been the low quality of the VO_2 films in sensors and devices. One experimental demonstration[21] with analysis[22] of a VO_2 microbolometer showed that superior performance is achievable under conditions of pulsed incident radiation with the sensor biased within the transition region. In another reported VO_2 microbolometer, the measured responsivity with the AC bias technique was 108 V/W.[8] The small responsivity was mainly attributed to the on-substrate design and low quality of the deposited VO_2 film on sapphire (resistance ratio around 10^4) with a large hysteresis (5 °C). The goal of our work is exploiting non-linear properties of VO_2 to create a hypersensitive mmWave sensor.

In our previous study, we presented the theoretical design of a highly sensitive antenna-coupled VO_2 microbolometer that operates in the transition region of VO_2.[23–25] In one aspect, the enhancement of the responsivity is based on the large TCR (171%/K)[25] within the MIT region of our high-contrast VO_2 thin film (1.46×10^4) on annealed alumina (Al_2O_3) buffer layer on silicon (Si) substrate.[3] Building on our prior work, we demonstrate the design, fabrication, and characterization of an antenna-coupled hyper-sensitive sensor using VO_2 films instead of VO_x which is biased with the voltage and temperature stimuli. Furthermore, the thermal performance of the device is improved by suspending the VO_2 sensor using deep reactive ion etching (DRIE) from the backside. We note that the phase transition temperature of VO_2 can be modified to room temperature which helps to reduce energy consumption for future designs. For instance, VO_2 films (3 to 20 nm) deposited by molecular-beam epitaxy exhibited a transition temperature of 290 ± 5 K.[26] Furthermore, thermal hysteresis of the MIT can be controlled by tuning the lattice constants of the W substituted VO_2.[27] Glassy type transition in VO_2 can prolong the MIT to room temperature as discussed in recent work.[28] To characterize the coupled dipole antenna and electrical properties of the VO_2 microbolometer in the mmWave band, we utilize an integrated coplanar waveguide (CPW) feed structure for excitation and biasing. By applying DC bias to the microbolometer in the non-linear MIT region, the large responsivity is achieved which is $>10^2$ times than the state-of-the-art sensors. Additionally, to validate the concept of the proposed hypersensitive VO_2 microbolometer for a mmWave imager, the antenna radiation pattern of the 4×4 antenna-coupled VO_2 microbolometer array is measured using the radar cross section (RCS) technique.

For microwave and mmWave bands, the microbolometer requires an antenna to receive the radiated power. From that point, the resistance of the sensitive material integrated in the microbolometer changes upon the electromagnetic power or temperature fluctuations. Electrical responsivity, which is a chief figure of merit, is studied to quantify the performance of the microbolometer and defined by the ratio of the output voltage change (ΔV) over the absorbed power (ΔP) as in

$$\Re = \frac{\Delta V}{\Delta P}. \tag{1}$$

$\Re$ can also be analytically expressed as[29]

$$\Re = I_b R \alpha \left| \frac{R_{th}}{1 + j2\pi f \tau} \right|, \tag{2}$$

where I_b is the bias current, R is the electrical resistance, α is the TCR, R_{th} is the thermal resistance, f is the modulation frequency, and τ is the transient response. The noise equivalent power (NEP) is another important figure of merit for the microbolometer and is defined as the ratio of the noise voltage over the responsivity: $NEP = S_n/\Re$. The noise voltage S_n consists of several sources: Johnson, phonon, and $1/f$ noises.[29]

Since responsivity is directly proportional to α as in (2), here, VO_2 is employed as the sensitive material in the proposed microbolometer design to take the advantage of the large TCR in the MIT region. Although there is a strong lattice match between single crystal C-plane sapphire and VO_2 thin film, sapphire cannot be widely implemented with the integrated circuits (IC) because of extremely low etch rates, lack of semiconductor properties, and difficulty in microfabrication processes. In a previous study, our group demonstrated the deposition of VO_2 thin films with a large electrical resistivity contrast on Si substrates for broader applications.[3] High quality VO_2 thin film is achieved by employing annealed atomic layer deposited (ALD) Al_2O_3 buffer layers that have crystalline properties similar to the bulk sapphire. The TCR of the highly oriented VO_2 can reach up to 171%/K in the phase transition region.[25] The proposed microbolometer architecture builds on our prior work on the deposition technique of VO_2 thin films. As demonstrated in Fig. 1, the VO_2 microbolometer is coupled to a dipole antenna and CPW with a target frequency range of 30–60 GHz representing the lower frequency portion of the mmWave band. The length and width of the designed antenna are 4.4 and 1.5 mm, respectively. The VO_2 sensor has dimensions $10 \times 60 \times 0.1\ \mu m^3$. The device is suspended on the Al_2O_3 buffer layer from the Si substrate to improve thermal isolation. More importantly, the antenna radiation efficiency is improved by removing the high-permittivity silicon substrate. The diameter of the main cutout of the Si substrate (dipole area) is 5 mm. The strategically placed fin and ring structures in Si are added to provide robust mechanical support for the membrane, sensor, and antenna.

The device is fabricated on a 4-in. 300-μm-thick double-side polished Si substrate. A 48-nm-thick Al_2O_3 thin film is grown by the

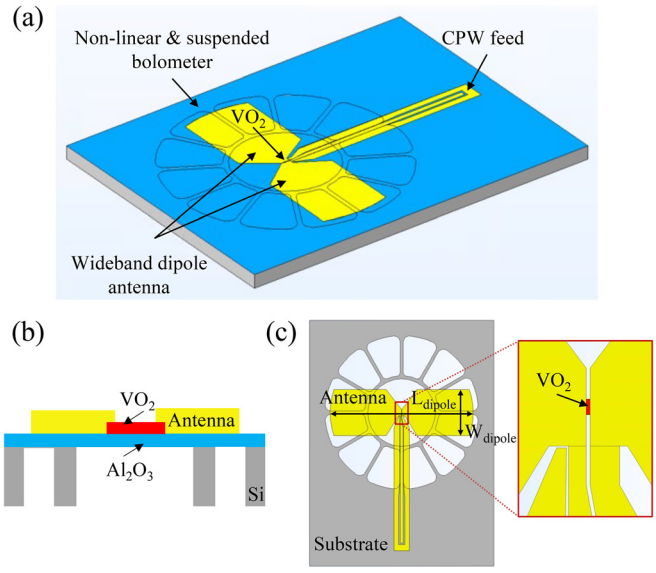

FIG. 1. (a) 3D schematic, (b) cross section, and (c) top view (without the Al_2O_3 buffer) of the antenna-coupled VO_2 microbolometer.

ALD technique on the Si substrate (Picosun Sunale R-150B ALD). Trimethylaluminum and H_2O are utilized as the precursors at 300 °C with N_2 purging gas. To have a better lattice match between VO_2 thin films and ALD Al_2O_3 thin films, as detailed in our previous work,[3] the amorphous ALD Al_2O_3 films are crystallized by the rapid thermal annealing (RTA) process which is carried out at a high temperature of 950 °C for 60 s in a N_2 ambient (AGA 410 RTA). The 100-nm-thick VO_2 thin film is then synthesized by DC sputtering from a vanadium metal target (AJA Orion RF/DC sputtering tool) in Ar plasma with 7.34% O_2,[3] including Ar plasma cleaning for the sample and chamber, sputtering deposition, and annealing. The measured temperature-dependent electrical resistivity of the deposited VO_2 thin film on annealed ALD Al_2O_3 is shown in Fig. 2 with detailed analyses previously reported in our work.[3] The electrical resistivity is sharp and nonlinear in the MIT region, which shows that a large resistance can be obtained even with a small temperature variance.

To pattern the VO_2 thin film for the device, positive photoresist Shipley S1813 is spin coated and patterned followed by the dry etch process using mixed SF_6 and Ar gases in an inductively coupled plasma reactive ion etching (ICP RIE) system (Plasma Therm SLR770). To fabricate the antenna, the image reversal photoresist AZ5214E is deposited and patterned on the sample. The e-beam evaporation process is carried out to deposit a 250-nm-thick Au layer (CHA Solution) followed by the liftoff process. The device is released by etching from the backside of the Si substrate. This is performed by patterning positive photoresist SPR220-7 with a DRIE process carried out in an ICP RIE system (Plasma Therm SLR770 ICP DRIE). After 390 cycles of etching with SF_6 and deposition with C_4F_8, 270–280 μm depth of the 300-μm-thick Si is etched with a small thickness (20–30 μm) left for mechanical robustness.

The DC performance as well as the radiation pattern of the fabricated devices are measured. The CPW-fed sensor is characterized for the antenna impedance match and detection properties, and the 4×4 sensor array is used to validate the radiation pattern for future imaging systems. The performance of the CPW-fed dipole antenna which is coupled to the VO_2 microbolometer ($10 \times 60 \times 0.1$ μm^3) is measured on the RF probe station (Cascade M150) shown in Fig. 3(b). A CPW

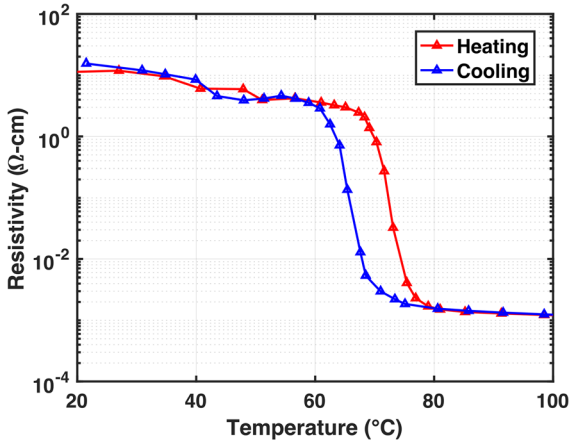

FIG. 2. Measured temperature-dependent electrical resistivity (with a contrast ratio of 1.46×10^4) of our VO_2 thin film on annealed ALD Al_2O_3 and the associated hysteresis.

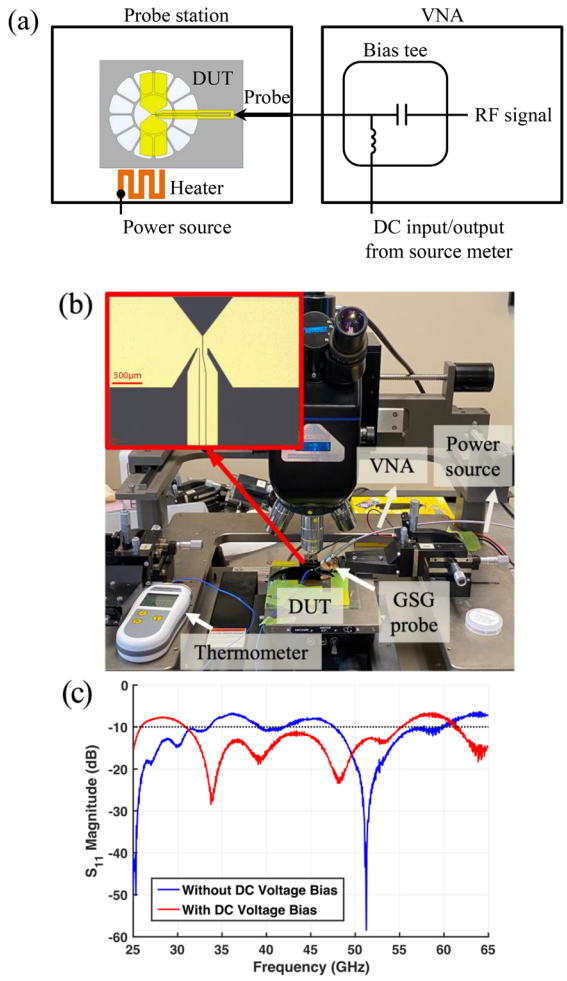

FIG. 3. (a) Illustration of test components. (b) The test setup for on-wafer measurement. (c) Measured reflection coefficient of CPW-coupled VO_2 microbolometer antenna.

calibration standards substrate is used prior to mmWave measurements. We directly apply the mmWave power to the microbolometer through the CPW by one port from the 67 GHz vector network analyzer (VNA), using a 150-μm pitch ground–signal–ground (GSG) 65 GHz probe (Infinity from FormFactor). Using the integrated bias tee of the VNA, the DC electrical signal can be applied with the same probe. The applied bias signals and the measured output signals are recorded using a source meter (Keysight B2901A). An external heater (Omega Engineering, Inc.) is used beneath the sample to activate the device near the phase transition region and emulate improved thermal conditions such as vacuum packaging that decrease the requirement for DC bias across the sensor. A DC voltage of 16.7 V is applied to the external heater using a power source (Keysight B2962A) and the surface temperature is measured to be 59.4 °C by a thermocouple temperature probe.

The impedance of the antenna is measured by the VNA through the CPW feed lines. Figure 3(c) demonstrates the reflection coefficient

(S_{11}) measured at 25–65 GHz. Before applying the DC voltage bias, VO_2 is at the dielectric phase and the antenna is not fully impedance matched in the design frequency range; it still, however, can absorb enough RF power to initiate response of the sensor. Once the DC voltage bias (7 V) tunes the microbolometer through the MIT, the frequency band with full impedance match (S_{11} lower than −10 dB) increases. The S_{11} results indicate the impedance change of the VO_2 microbolometer when it enters and subsequently passes through the transition region with the DC voltage bias. The wideband design of the antenna gives robustness to the impedance match even as the sensor's resistance changes sharply. As illustrated in Fig. 3(c), the CPW-coupled antenna is measured to exhibit impedance match of $S_{11} \leq -10$ dB from 31 to 55 GHz when the DC bias induces the MIT of VO_2. In practice, the antennas act as receivers, but with the experimental setup, it is convenient to use reciprocity to treat them as transmitters.

We also measured the radiation pattern of the 4×4 antenna-coupled VO_2 microbolometer array. Here, we use a RCS technique, which is a non-contact backscattering approach. RCS corresponds to target gain factor and, therefore, to antenna gain. For proof of concept of our array, the antennas are not coupled to any transmission line, emulating the case of a fully realized imaging array. However, as there is no readout integrated circuit (ROIC) available at this stage to bias the VO_2, the antenna elements' impedance match due to VO_2 conductivity is not controlled via a DC bias; therefore, the VO_2 resistors during RCS measurements are at room temperature (insulating state) with resistance ∼100 kΩ, giving high reflection ($S_{11} \approx 0$ dB). A high reflection coefficient is preferred in the case of RCS measurement to maximize radiation backscattered to the receiving (R_x) horn antenna. The VO_2 geometry is adjusted for the array to be $10 \times 200 \times 0.1\ \mu m^3$, so that in a full ROIC-controlled device, temperature and DC bias can be used to set the initial VO_2 impedance at ∼75 Ω, which will then change in response to incoming RF power level.

This non-contact method is utilized to replace the cables and probes for the antenna gain measurement at the mmWave band similar to our prior work in testing 60 GHz antenna arrays.[30,31] Here, we use a six-axis robot system (Fanuc LR Mate200iD) developed in our previous study[32,33] with a dual-horn monostatic radar setup to measure radiation pattern, shown in Fig. 4(a). This setup is used due to the high complexity of measuring probed radiating elements, which requires extensive experimental design and equipment outside the scope of this project. The horns are placed in a 3D printed fixture attached to the robot at the end of the manipulator, with a toe-in angle between the horns of 6.9°. To reduce mutual coupling between the horn antennas, flat absorber foam is placed around the opening of the horns.[34] The transmission coefficient from the transmitting horn antenna to the receiving horn antenna, S_{21}, is obtained by the VNA during the trajectory. Before the device measurement, the standard gain horn antennas (QSH-SL−50-75-V-20) are used to establish signal floor by scanning the test setup. The transmission coefficient in this reference scan is below –70 dB; peak S_{21} with antenna array present is −43 dB. The 4×4 VO_2 microbolometer array is visually aligned with the horn antennas using a laser pointer, and S-parameter measurements are taken in a half-circle trajectory with 0.33° angular resolution at a radius R = 350 mm from the end of the robot arm. Given that distance, horn antenna gain, and wavelength are constant, target gain factor varies only with excitation angle, normalized antenna gain is proportional to S_{21}.

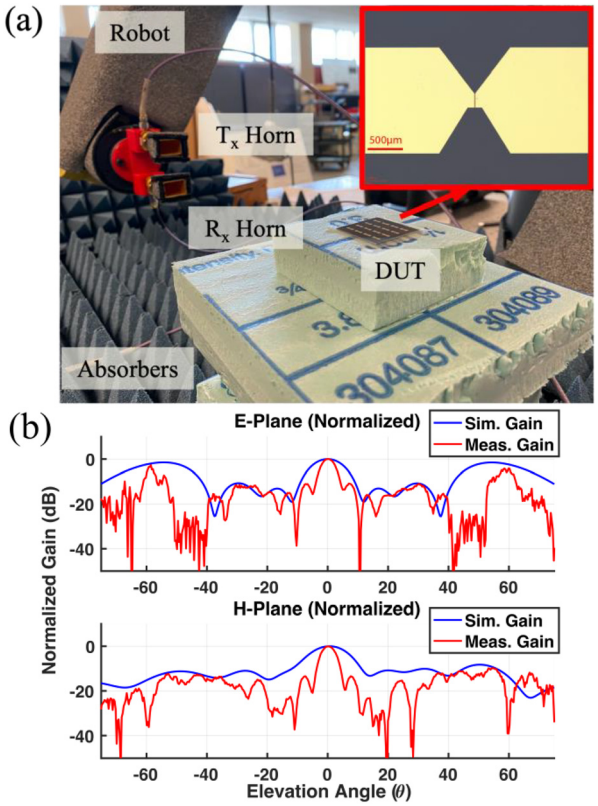

FIG. 4. (a) The test setup for RCS measurement. The angle between the horn antennas is 6.9°. (b) The normalized gain pattern of the 4×4 VO_2 microbolometer array in the E-plane and H-plane.

The normalized gain pattern at 60 GHz in E-plane and H-plane is shown in Fig. 4(b). Peak gain is at 0° with sidelobes at ±20°–30° and ±60° in the E-plane and broad sidelobes from ±20° to 60° in the H-plane. Simulations are performed for comparison to measurement using the ANSYS HFSS finite array tool. For simplicity, the array is simulated as though it is radiating elements; by the principle of electromagnetic time reversal, this gives the same result as would simulation of receiving elements. It was determined that reflections directly due to the Si substrate contribute significantly to this pattern at the central angles, ±15°, resulting in a narrower mainlobe and lower sidelobe levels than in the simulated array. Nevertheless, the relative profile of the RCS gain pattern shows reasonable agreement in the sidelobes, provisionally verifying the array pattern between simulation and measurement. The measured curves given in Fig. 4(b) are adjusted by $n(2 - \cos 2\theta)$, with $n = 2.5$ in E plane and $n = 1.5$ in H plane to account for the RCS contributions at the central angles from the Si substrate. When the outer sidelobes are brought in line with the simulated sidelobes, the inner sidelobes follow similarly, therefore validating the compensating curve. In a fully realized imaging system, the antenna array would receive collimated radiation from a specialized lensing and masking system, therefore only at the broadside angle; therefore, the high sidelobes can be blocked so as not to be detrimental to the system.

The static (steady state) I–V characterization of VO_2 microbolometer is obtained when applying the RF signal between 25 and 65 GHz varied by the VNA. The transition of the VO_2 resistor is triggered by the DC bias and the RF power absorbed. Figure 5(a) shows the I–V plot with different RF power input ranging from −25 to 0 dBm (3.1 μW to 1 mW). For each power level applied by the VNA, the double-sweep voltage bias is applied to the VO_2 microbolometer and the corresponding current is measured by the source meter. As shown in Fig. 5(a), the I–V curves are highly non-linear. With the increase in the voltage bias, VO_2 starts from the linear dielectric phase. Then, there is a sharp increase in the current which indicates the MIT region of VO_2 and the resistance decreases and moves quickly through the value of ∼248 Ω. As the voltage further increases, VO_2 enters the linear conductive region with a resistance of ∼89 Ω. When the voltage decreases, the hysteresis phenomenon is evident, and finally, VO_2 transforms back to the dielectric state. In addition, it is demonstrated in Fig. 5(a) that with the increase in the RF input power, the required voltage to trigger MIT decreases (shifts to the left). The shift of the threshold voltage confirms that the device can sense the power change as low as −25 dBm. The relationship between the input power and the critical voltage to induce the MIT is shown in Fig. 5(b). The phenomenon that different levels of external power influence the threshold voltage is a significant demonstration of our VO_2 sensor.

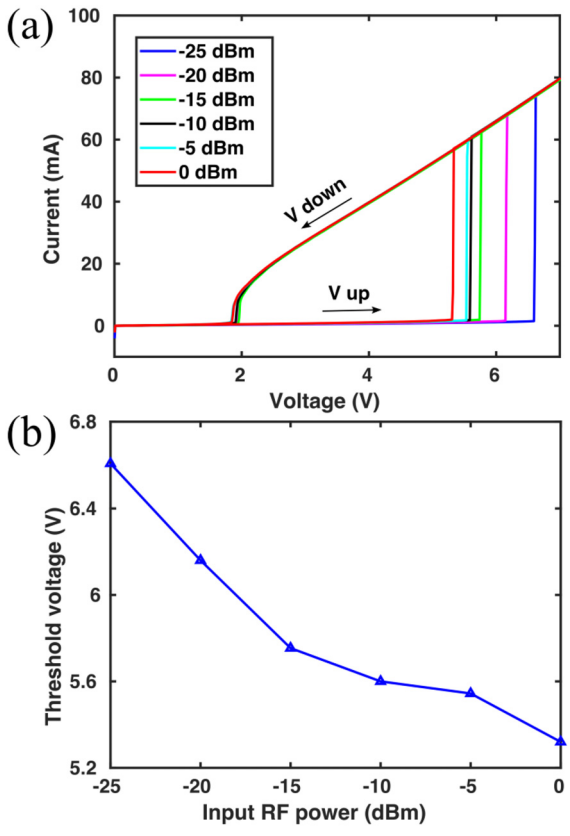

FIG. 5. I–V curve of the VO_2 microbolometer with different applied RF power. (b) Threshold voltage vs various input RF power.

Responsivity is the primary figure of merit to characterize the microbolometer's performance as in (1). In this case, the DC responsivity can be estimated from the ratio of the shift in the required voltage for the MIT over the input power change to the VO_2 microbolometer. The DC responsivity is extracted from the threshold voltage shift over the corresponding RF power change to the VO_2 microbolometer, shown in Fig. 6. It can be observed that the responsivity is highly non-linear and has a larger value with a smaller RF power change. This is mainly due to the non-linear resistivity (or TCR) of VO_2 in the MIT region. Considering the TCR value in the transition region and the limitations of the measurement setup, the responsivity is expected to reach a plateau at low input power levels. Below 3.1 μW level, there was noise in the instrumentation overpowering the signal, making the readout unstable, unrecognizable, and inaccurate compared to the larger power levels. These low power levels gave an inconclusive result that could not be considered for inclusion. The maximum DC responsivity of our sensor is 6.55×10^4 V/W. The NEP is calculated considering the Johnson and phonon noises since the $1/f$ noise depends on aspects related to the fabrication process[35] and can be neglected at the high frequency (100 kHz).[36] The thermal resistance of the microbolometer is analytically estimated to be $R_{th} = 6 \times 10^3$ K/W.[25] The Johnson noise voltage and phonon noise voltage are 2.133×10^{-9} and 2.088×10^{-6} $V/\sqrt{Hz}$, respectively.[29] The phonon noise is dominant in the total noise of the microbolometer due to the large responsivity. The NEP is estimated to be 31.88 $pW/\sqrt{Hz}$. The measured high responsivity is $>10^2$ times larger than the state-of-the-art antenna-coupled microbolometers that use materials with small TCR[37–40] as shown in Table I. The key aspects in the enhancement of the responsivity include the utilization of VO_2's large TCR in the MIT region and good thermal isolation by the suspension. Compared with extracting the voltage change with a current bias we presented previously,[25] the DC voltage bias method has the advantage of demonstrating the shift in VO_2's activation voltage in response to steady RF input power, with less stringent requirement for bias precision. The DC voltage bias is swept up and down across the transition region rather than held steady within the transition cliff. Because the voltage for activation of VO_2 changes depending on temperature, the shifts in activation voltage due to changes in RF input power can be paired with known temperature values. This can be used for

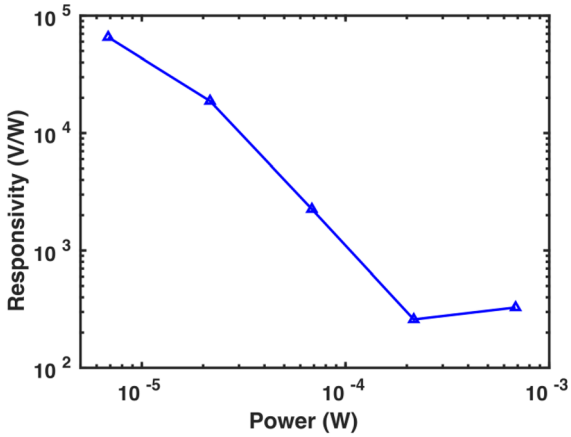

FIG. 6. DC responsivity due to various applied RF power change.

TABLE I. Comparison of antenna-couped microbolometers.

	Material	Dimension (μm^3)	Responsivity (V/W)
This work	VO_2	$10 \times 60 \times 0.1$	6.55×10^4
37	Nb	$10 \times 1 \times 0.035$	85
38	$PrBa_2Cu_3O_{7-x}$	$2 \times 5 \times 0.07$	33
39	Ti	$19.72 \times 0.1 \times 0.046$	255
40	$Mn_{1.56}Co_{0.96}Ni_{0.48}O_4$	$200 \times 40 \times 10$	440.2

measurement on its own, or it can be used along with known RF input power to calibrate for temperature in a mmWave camera that would employ either voltage or current bias at the phase transition cliff.

In this work, we report the realization of an antenna-coupled VO_2 microbolometer that operates in the phase transition region. The overall performance of the VO_2 microbolometer is enhanced by bulk micromachining suspension technique and biasing the device in VO_2's MIT with a large TCR. In RF probe measurement, the frequency band of the coupled dipole antenna was 31–55 GHz. Additionally, the gain pattern of the 4×4 VO_2 microbolometer array was obtained by the RCS approach. DC/RF measurement results demonstrate an ultra-high responsivity (6.55×10^4 V/W). The presented work exhibits the potential and advantage of employing VO_2 as the sensitive material for the antenna-coupled microbolometer to achieve a large responsivity for mmWave imaging.

This material is based upon the work supported by the U.S. National Science Foundation (NSF) CAREER Award under Grant Nos. 1845370 and 2149886, the Air Force Research Lab (AFRL)/Defense Associated Graduate Student Innovators (DAGSI) Award No. RY6-OSU-19-2-AFRL2, and AFOSR Lab Task 21RYCOR019 supported by Dr. Ilya Vitebskiy.

AUTHOR DECLARATIONS

Conflict of Interest

The authors have no conflicts to disclose.

Author Contributions

Shangyi Chen: Data curation (lead); Formal analysis (lead); Methodology (lead); Writing – original draft (lead); Writing – review & editing (lead). **Mark Lust:** Data curation (supporting); Validation (supporting); Writing – original draft (supporting); Writing – review & editing (supporting). **Nima Ghalichechian:** Conceptualization (lead); Funding acquisition (lead); Supervision (lead); Writing – original draft (supporting); Writing – review & editing (supporting).

DATA AVAILABILITY

The data that support the findings of this study are available within the article.

REFERENCES

[1]M. K. Sohn, H. Singh, E.-M. Kim, G. S. Heo, S. W. Choi, D. G. Phyun, and D. J. Kang, Appl. Phys. Lett. **120**(17), 173503 (2022).
[2]V. Sanphuang, N. Ghalichechian, N. K. Nahar, and J. L. Volakis, Appl. Phys. Lett. **107**(25), 253106 (2015).
[3]M. Lust, S. Chen, C. E. Wilson, J. Argo, V. Doan-Nguyen, and N. Ghalichechian, J. Appl. Phys. **127**(20), 205303 (2020).
[4]S. P. Langley, Proc. Am. Acad. Arts Sci. **16**, 342 (1880).
[5]F. Niklaus, C. Vieider, and H. Jakobsen, in *MEMS/MOEMS Technologies and Applications III* (SPIE, Beijing, 2008), Vol. 6836, p. 68360D.
[6]M. E. MacDonald and E. N. Grossman, IEEE Trans. Microwave Theory Techn. **43**(4), 893 (1995).
[7]M. Moreno, R. Jiménez, A. Torres, and R. Ambrosio, IEEE Trans. Electron Devices **62**(7), 2120 (2015).
[8]C. D. Reintsema, E. N. Grossman, and J. A. Koch, in *Infrared Technology and Applications XXV* (International Society for Optics and Photonics, Orlando, FL, 1999), Vol. 3698, p. 190.
[9]A. H. Lettington, D. Dunn, M. Attia, and I. M. Blankson, J. Opt. A **5**(4), S103 (2003).
[10]M. T. Ahmad Beig, M. Kumar, Y. Sharma, and B. K. Sharma, J. Phys. **2335**(1), 012005 (2022).
[11]R. Appleby, D. Gleed, R. Anderton, and A. Lettington, Opt. Eng. **32**(6), 1370 (1993).
[12]L. Yujiri, M. Shoucri, and P. Moffa, IEEE Microwave Mag. **4**(3), 39 (2003).
[13]V. Y. Zerov and V. Malyarov, J. Opt. Technol. **68**(12), 939 (2001).
[14]A. R. Luukanen, S. Vaijaervi, and H. Sipila, in *Passive Millimeter-Wave Imaging Technology IV* (SPIE, Orlando, FL, 2000), Vol. 4032, p. 81.
[15]I. Kašalynas, R. Venckevičius, L. Minkevičius, A. Sešek, F. Wahaia, V. Tamošiūnas, B. Voisiat, D. Seliuta, G. Valušis, A. Švigelj, and J. Trontelj, Sensors **16**(4), 432 (2016).
[16]C. Middleton, G. Zummo, A. Weeks, A. Pergande, L. Mirth, and G. Boreman, in *Infrared and Millimeter Waves, Conference Digest of the 2004 Joint 29th International Conference on 2004 and 12th International Conference on Terahertz Electronics* (SPIE, Orlando, FL, 2004), Vol. 5410, p. 745.
[17]T. Uchida, A. Matsushita, and T. Tachiki, IEEJ Trans. Electr. Electron. Eng. **13**(6), 876 (2018).
[18]S. Yoneoka, M. Liger, G. Yama, R. Schuster, F. Purkl, J. Provine, F. B. Prinz, R. T. Howe, and T. W. Kenny, in *2011 IEEE 24th International Conference on Micro Electro Mechanical Systems* (IEEE, Cancun, 2011), p. 676.
[19]W. A. Radford, D. F. Murphy, A. Finch, A. Kennedy, J. Kojiro, M. Ray, R. Wyles, R. Coda, E. A. Moody, and S. T. Baur, in *Infrared Detectors and Focal Plane Arrays V* (International Society for Optics and Photonics, San Diego, CA, 1998), Vol. 3379, p. 22.
[20]D. Murphy, M. Ray, J. Wyles, C. Hewitt, R. Wyles, E. Gordon, K. Almada, T. Sessler, S. Baur, and D. Van Lue, in *Infrared Technology and Applications XXXIII* (International Society for Optics and Photonics, Orlando, FL, 2007), Vol. 6542, p. 65421Z.
[21]V. Y. Zerov, Y. V. Kulikov, V. Leonov, V. Malyarov, I. Khrebtov, and I. Shaganov, J. Opt. Technol. **66**(5), 387 (1999).
[22]L. De Almeida, G. Deep, A. Lima, I. Khrebtov, V. Malyarov, and H. Neff, Appl. Phys. Lett. **85**(16), 3605 (2004).
[23]S. Chen, B. Ghassemiparvin, and N. Ghalichechian, in *2018 12th European Conference on Antennas and Propagation (EuCAP)* (IET Digital Library, London, 2018), p. 1.
[24]S. Chen, M. Lust, and N. Ghalichechian, in *2019 IEEE International Symposium on Antennas and Propagation and USNC-URSI Radio Science Meeting* (IEEE, Atlanta, GA, 2019), p. 1641.
[25]S. Chen, M. Lust, and N. Ghalichechian, Microsyst. Technol. **27**(7), 2815 (2021).
[26]H. Paik, J. A. Moyer, T. Spila, J. W. Tashman, J. A. Mundy, E. Freeman, N. Shukla, J. M. Lapano, R. Engel-Herbert, W. Zander, J. Schubert, D. A. Muller, S. Datta, P. Schiffer, and D. G. Schlom, Appl. Phys. Lett. **107**(16), 163101 (2015).
[27]Y. G. Liang, S. Lee, H. S. Yu, H. R. Zhang, Y. J. Liang, P. Y. Zavalij, X. Chen, R. D. James, L. A. Bendersky, A. V. Davydov, X. H. Zhang, and I. Takeuchi, Nat. Commun. **11**(1), 3539 (2020).
[28]G. Wei, X. Fan, Y. Xiong, C. Lv, S. Li, and X. Lin, Appl. Phys. Express **15**(4), 043002 (2022).
[29]H.-H. Yang and G. M. Rebeiz, IEEE Trans. Microwave Theory Techn. **63**(11), 3760 (2015).

[30]J. Li, C. Matos, S. Chen, and N. Ghalichechian, IEEE Antennas Wireless Propag. Lett. **20**(4), 473 (2021).
[31]J. Li, C. Matos, and N. Ghalichechian, IEEE Antennas Wireless Propag. Lett. **20**(4), 513 (2021).
[32]C. Matos, J. Li, and N. Ghalichechian, in *2019 Antenna Measurement Techniques Association Symposium (AMTA)* (IEEE, San Diego, CA, 2019), p. 1.
[33]C. Matos, J. Humanchuk, and N. Ghalichechian, Microwave Opt. Technol. Lett. **63**(5), 1520 (2021).
[34]N. Michishita, T. Chisaka, and Y. Yamada, in *2013 Proceedings of the International Symposium on Antennas & Propagation* (IEEE, Nanjing, 2013), Vol. 01, p. 400.
[35]Q. Cheng, S. Paradis, T. Bui, and M. Almasri, IEEE Sens. J. **11**(1), 167 (2011).
[36]D. Neikirk, W. W. Lam, and D. Rutledge, Int. J. Infrared Millimeter Waves **5**(3), 245 (1984).
[37]A. J. Miller, A. Luukanen, and E. N. Grossman, in *Terahertz for Military and Security Applications II* (SPIE, Orlando, FL, 2004), Vol. 5411, p. 18.
[38]A. Scheuring, P. Thoma, J. Day, K. Il'in, J. Hanisch, B. Holzapfel, and M. Siegel, IEEE Trans. Terahertz Sci. Technol. **3**(1), 103 (2013).
[39]A. Tiwari, H. Satoh, M. Aoki, M. Takeda, N. Hiromoto, and H. Inokawa, Int. J. ChemTech Res. **7**, 1019 (2015).
[40]T. Hu, W. Ma, J. Wu, Z. Zhang, W. Zhou, N. Yao, Q. Qiu, and Z. Huang, Appl. Phys. Express **13**(12), 124002 (2020).